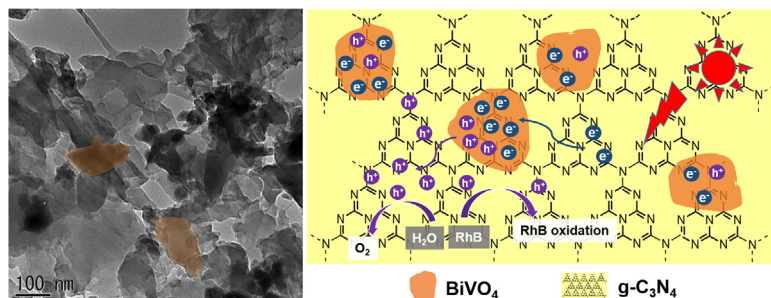




Regular Article

Construction of 2D/2D BiVO₄/g-C₃N₄ nanosheet heterostructures with improved photocatalytic activityZhichao Sun^{a,b}, Zhiquan Yu^b, Yingya Liu^{a,b}, Chuan Shi^a, Mingshan Zhu^{c,*}, Anjie Wang^{a,b,*}^a State Key Laboratory of Fine Chemicals, Dalian University of Technology, Dalian 116024, PR China^b Liaoning Key Laboratory of Petrochemical Technology and Equipments, Dalian University of Technology, Dalian 116024, PR China^c Guangdong Key Laboratory of Environmental Pollution and Health, School of Environment, Jinan University, Guangzhou 510632, PR China

GRAPHICAL ABSTRACT



ARTICLE INFO

Article history:

Received 15 June 2018

Revised 14 August 2018

Accepted 22 August 2018

Available online 23 August 2018

Keywords:

2D/2D

BiVO₄g-C₃N₄

Heterostructure

Photocatalysis

ABSTRACT

In this work, a two dimensional (2D)/2D BiVO₄/g-C₃N₄ heterostructure with strong interfacial interaction was successfully constructed. The as-prepared BiVO₄/g-C₃N₄ heterostructures exhibit distinctly enhanced visible light photocatalytic performance toward the degradation of Rodanmin B (RhB) and water splitting to oxygen (O₂) as compared to pristine g-C₃N₄ and BiVO₄, which can be attributed to the strong interfacial interaction and abundant 2D coupling interfaces, facilitating efficient charge separation. Among the composites with various ratios, the BiVO₄-10/g-C₃N₄ sample achieves the optimum photocatalytic activity for the degradation of RhB, and reached 15.8 and 4.3 times compared to pure g-C₃N₄ and BiVO₄. Moreover, the corresponding composite reached a high O₂-production rate of 0.97 μmol h⁻¹ under visible light irradiation, which is 12.1 and 2.8 times higher than that of pure g-C₃N₄ and BiVO₄, respectively. It was demonstrated that the efficiency of electron-hole separation has certain contribution to the photocatalytic performance over the BiVO₄/g-C₃N₄ heterostructure. The present study suggests that the unique 2D/2D BiVO₄/g-C₃N₄ hybrid nanosheets should be conducive to improve the photocatalytic performance of organic pollutant degradation and water splitting.

© 2018 Elsevier Inc. All rights reserved.

* Corresponding authors at: State Key Laboratory of Fine Chemicals, Dalian University of Technology, Dalian 116024, PR China (A. Wang).

E-mail addresses: mingshanzhu@yahoo.com (M. Zhu), ajwang@dlut.edu.cn (A. Wang).

1. Introduction

Semiconductor photocatalyst is a potential material to solve the pollution degradation by utilizing solar energy [1–4]. Therefore, great deals of attention have been received to exploit high efficient photocatalytic semiconductor capable of responding to visible light. Various types' photocatalysts with different morphology

have been developed to improve the light response range and quantum efficiency [5–7]. Among the geometry of composite material, the 2D/2D heterojunction often shows the excellent separation of electron–hole pairs due to the intimate face-to-face contact as compared to the point-to-face contact in the 0D/2D heterojunction and the line-to-face contact in the 1D/2D heterojunction, which might lead to the enhanced photocatalytic activity [8,9].

Bismuth based semiconductor has received significant interest due to its unique physical properties [10–12]. BiVO₄ is one of the most outstanding photocatalysts with an appropriate direct band gap of 2.4 eV for absorbing visible light [13]. However, the high recombination of photo-induced electron and hole is an obstacle to achieve an efficient photocatalytic performance. It is generally believed that coupling two or more semiconductors can reduce the recombination of photo-generated electron-hole pairs [14,15]. Graphitic carbon nitride (g-C₃N₄) is an encouraging candidate material with a suitable bandgap (2.7 eV) and 2D nanosheet structure [15–20]. A series of works have indicated that the appropriate band structure of BiVO₄ and g-C₃N₄ can promote the photocatalytic activity due to the efficient photo-induced electron-holes transferring and separation between BiVO₄ and g-C₃N₄ [21]. It is known that the synergistic effect between BiVO₄ and g-C₃N₄ would be associated with their external morphology, which could significantly influence the photocatalytic performance [22,23]. In particular, 2D/2D multilayered hybrid nanosheets possess a much larger contact area compared to 2D/0D or 2D/1D nanomaterials that are only in point-to-point or line-to-line contact [24,25]. Thus, the larger contact interfaces between 2D/2D composite provide more effective separation of photo-generated electron-hole pairs and outstanding photocatalytic performance. Recently, various morphological types of BiVO₄, such as bulk [26–28], nanorods [29], regular polyhedral structures [30,31], leaf-like nanostructures [32], agglomerated particles [33], as well as platelet-like morphologies [34], are used to be hybridized with nanosheet g-C₃N₄. However, to the best of our knowledge, no attempt has been made on construction of 2D/2D heterostructure with ultrathin nanosheet BiVO₄ and nanosheet g-C₃N₄, this has motivated us to take up the present study.

In this work, 2D nanosheet of BiVO₄ with 20–30 nm thickness was synthesized and combined with the 2D nanosheet of g-C₃N₄ to form a heterostructure with 2D/2D morphology. The photodegradation of Rhodamine B (RhB) and water splitting to oxygen (O₂) were examined under visible light irradiation. All of the composite material, except BiVO₄-40/g-C₃N₄ exhibits an enhanced performance to pristine g-C₃N₄ and BiVO₄. Among them, BiVO₄-10/g-C₃N₄ showed the highest photocatalytic activity. Electrochemical Impedance Spectroscopy (EIS) and photocurrent confirmed the efficient electron transfer between BiVO₄ and g-C₃N₄, which may be due to the large interface region of 2D/2D structure. These current results may provide a new insight to build 2D/2D heterojunction photocatalyst with effective charge separation, which show a great potentiality in the application of water purification and water splitting.

2. Experimental

2.1. Chemicals

Bismuth nitrate pentahydrate (Bi(NO₃)₃·5H₂O), ammonium metavanadate (NH₄VO₃), sodium dodecyl benzene sulfonate (SDBS), Nitric acid (65–68%), Sodium hydroxide (NaOH), N,N-Dimethylformamide (DMF), urea (H₂NCONH₂), Rhodamine B (RhB) Cobalt nitrate hexahydrate (Co(NO₃)₂·6H₂O), hydrogen peroxide (H₂O₂), silver nitrate (AgNO₃), ammonia aqueous solution

(25 wt%), sodium sulfate (Na₂SO₄) and ethanol were purchased from Sinopharm Chemical Reagent Co. Ltd. (China) and used without further purification. Nafion was provided by Sigma-Aldrich Chemicals Corporation. The water used in this study was deionized and purified through a water purification system (resistivity: ~18 MΩ cm).

2.2. Synthesis of g-C₃N₄ nanosheets

g-C₃N₄ nanosheets was prepared by thermally method under a static atmosphere [16]. 5 g of urea was placed in an alumina crucible with a cover and kept at 550 °C for 2 h with a heating rate of 2 °C min⁻¹. The obtained yellowish resultant was collected and ground into fine powder as the final product.

2.3. Synthesis of BiVO₄ nanosheets

The BiVO₄ nanosheets were prepared by a hydrothermal method [35]. 1.2250 g of Bi(NO₃)₃·5H₂O and 0.2900 g of NH₄VO₃ was dissolved into 5 mL of 4.0 M HNO₃ and 2.0 M NaOH to obtain a pellucid solution, respectively. 0.1250 g of SDBS was then added into both of the above solutions with vigorous stirring for 0.5 h. After that, the two solutions were mixed to give a bisque solution under stirring, followed by an addition of 2.0 M NaOH to adjust the pH value to 7.0. After stirring for another 0.5 h, the mixture was transferred into a Teflon-lined stainless steel autoclave until 80% of the volume of the autoclave was occupied. The autoclave was heated in an oven at 200 °C for 4 h, and allowed to cool down to room temperature. The vivid yellowish precipitate was washed with distilled water and collected by centrifugation, and then dried at 100 °C for 4 h.

2.4. Synthesis of 2D/2D BiVO₄/g-C₃N₄ heterostructure

Four samples of g-C₃N₄ hybrid with BiVO₄ with different BiVO₄/g-C₃N₄ mass ratio were prepared. In a typical process, a certain amount of g-C₃N₄ was dissolved into 20 mL of DMF and held for 15 min under ultrasound. Then, a given amount of BiVO₄ was dispersed into the suspension solution under ultrasound for 1 h and stirring for another 12 h. The resultant solution was separated by centrifugation, washed repeatedly with water and ethanol, and dried at 60 °C for 6 h. The final hybrid was signed as BiVO₄-z/g-C₃N₄, where z represents the mass percentage of BiVO₄.

2.5. Photocatalytic performance

Photodegradation experiments were performed in a quartz bottle (50 mL) at ambient temperature. In a typical experiment, 10 mg of the obtained photocatalyst was suspended in 20 mL 20 mg/L RhB aqueous solution. Before a consistent activity test, the system was kept for 30 min in the darkness under vigorous stirring to achieve an adsorption–desorption equilibrium condition. All the photocatalytic measurements were performed on a 300 W Xenon arc lamp (CEL-PF300-T8, Beijing China Education Au-light Co., Ltd). The light was cut through by a UV cutoff filter (>420 nm) before entering the reactor. The absorbance of RhB was measured by UV spectrometer (JASCO UV-550 spectrophotometer) at 554 nm after centrifugation. The degradation efficiency (%) was calculated by using the following equation:

$$\text{Degradation E (\%)} = (C_0 - C)/C_0 \times 100\%$$

where C₀ represents the concentration of RhB before irradiation process, and C represents the time dependent concentration of RhB upon irradiation process.

2.6. Photocatalytic water splitting

5 mg samples were dispersed into 8 mL H₂O solution, and then added into a 35 mL cylinder reactor and sealed with a rubber septum. The system was deaerated by Ar bubbling into the dispersion for 30 min. Before photoreactions, the dispersion was sonicated for 5–10 min. Afterwards, the system was stirring continuously and irradiating under visible light by using Xenon lamp (CEL-PF300-T8, Beijing China Education Au-light Co., Ltd) with a 420 nm cut-off filter. The gases produced were analyzed with a gas chromatograph (Agilent 7890) equipped with an MS-5A column and a thermal conductivity detector (TCD). For the half reaction, AgNO₃ (4 mL, 0.1 M) was used for photocatalytic O₂ production.

2.7. Characterization

The crystalline structures of the as-prepared samples were characterized by X-ray diffraction (XRD, Rigaku D/Max 2400 diffractometer with nickel-filtered Cu-K α radiation at 40 kV and 100 mA). Chemical compositions of the samples were examined by X-ray photoelectron spectroscopy (Multilab 2000 X-ray photoelectron spectrometer, using an Mg-K α source). SEM and EDX were tested by a Nova NanoSEM 450, FEI Company, USA, acceleration voltage of 3.0 kV. TEM and HRTEM were achieved by a FEI Tecnai G2 F30 transmission microscope operated at 300 kV. The UV–vis absorption and diffuse reflectance spectra were measured by JASCO UV-550 spectrophotometer. The photoelectrochemical measurements were recorded on a BAS-100 W electrochemical potentiostat in a three-electrode cell. The room-temperature photoluminescence (PL) spectra were investigated using a fluorescence spectrometer (Hitachi F-7000) equipped with a 150 W Xe lamp.

3. Results and discussion

The crystalline structure of g-C₃N₄, BiVO₄ and the hybrid samples was analyzed by X-ray powder diffraction (XRD). As shown in Fig. 1, a number of characteristic peaks at 2 θ angles of 28.6°, 28.8°, 28.9°, 30.5°, 46.7°, 47.3°, 53.2°, and 53.3°, could be well-indexed to the (–1 3 0), (–1 2 1), (1 2 1), (0 4 0), (2 4 0), (0 4 2), (–1 6 1), and (1 6 1) lattice plane of phase-pure BiVO₄ crystallites (JCPDS file 14-0688), respectively [36]. No peaks of other phases or impurities were detected for pristine BiVO₄. The diffraction patterns of BiVO₄ reveal sharp and intense peaks, which demonstrate

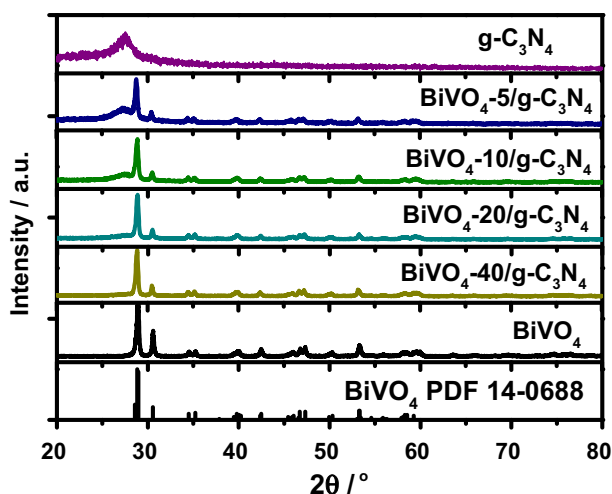


Fig. 1. XRD patterns of as-prepared BiVO₄, g-C₃N₄, and BiVO₄/g-C₃N₄.

the high crystallinity of pure sample. The g-C₃N₄ was evidenced by a broad peak at 27.4° of 2 θ , which is representative for a typical interplanar stacked graphitic layered structure [37,38]. The as-prepared BiVO₄/g-C₃N₄ composite was well demonstrated with the detection of both phases of g-C₃N₄ and BiVO₄ and without other detectable impurities. The sample with high ratio of BiVO₄/g-C₃N₄ shows mainly a BiVO₄ phase, with a fraction of g-C₃N₄ hardly detectable. As the ratio of g-C₃N₄ is increased, the diffraction peak belongs to g-C₃N₄ shows higher intensity.

The morphologies and microstructures of BiVO₄/g-C₃N₄ samples were analyzed by field emission scanning electron microscopy (FESEM), transmission electron microscopy (TEM) and high resolution TEM (HRTEM). SEM images confirmed the sheet shape of all as-prepared samples. It is evident from the Fig. 2(a) and (b) that the pure BiVO₄ and g-C₃N₄ both exhibit well-defined ultrathin 2D sheet-like morphology. The pure BiVO₄ composed of a large number of thin plat features with a thickness of 20–30 nm and pure g-C₃N₄ showed a rippled and crumpled nanosheet with certain porosity. As shown in Fig. 2(c), BiVO₄/g-C₃N₄ composites possess a curly paper-like structure attached with some thin plats, forming a 2D sheet-on-sheet architecture. Such a unique structure features large interfacial contacts between layered BiVO₄ and g-C₃N₄ nanosheets, favoring faster electron transfer, compared with other 0D/2D and 1D/2D structures.

Further insights into the morphology of the hybrid nanosheets were obtained from TEM and HRTEM images. The TEM images of BiVO₄, g-C₃N₄, and BiVO₄/g-C₃N₄ were shown in Fig. 3. Fig. 3(a) clearly shows that the as-prepared BiVO₄ has a 2D sheet-like and plat morphology, which is consistent with the results of FESEM images. The g-C₃N₄ also shows large and ultrathin 2D nanosheet structure (Fig. 3(c)). The TEM image of the hybrid material, as shown in Fig. 3(d), composed of two ultrathin 2D lamellars adhere to one another. The unique 2D/2D layered structure of the BiVO₄/g-C₃N₄ hybrid nanosheets can increase the contact area between the two materials, which would enhance the electron transfer and the photocatalytic activity of the hybrid. The HRTEM image shows that the pure BiVO₄ nanosheets with a characteristic lattice spacing of 0.292 nm was matched well with the typical (0 4 0) plane of BiVO₄ (Fig. 3(b)). No obvious crystal fringe was observed for g-C₃N₄ nanosheets, due to the amorphous structure. The characteristic lattice spacing of 0.292 nm was also observed in the composite specimen (Fig. 3(e)), which confirms the combination between BiVO₄ and g-C₃N₄.

Energy dispersive X-ray detector (EDX) was used to validate the composition of BiVO₄, g-C₃N₄, and BiVO₄/g-C₃N₄ (Fig. S1). The EDX microanalysis shows clearly that the pure BiVO₄ was consists of Bi, V, and O, with a stoichiometric atomic ratio of 1:1.04:3.88. For g-C₃N₄ sample, C and N elements could be evidently detected and the atomic ratio between C and N elements is approximately 1:1.43, which is lightly higher than the theoretic stoichiometric atomic ratio of 1:1.33. The typical EDX pattern for BiVO₄/g-C₃N₄ show a clear signal of the presence of Bi, V, O, C, and N, with no other elements detected. These results, together with XRD and TEM images confirm the composite specimen was composed of BiVO₄ and g-C₃N₄.

The optical absorption properties were investigated by UV–Vis spectroscopy. The UV–Vis diffuse reflectance spectra (UV–Vis DRS) of all samples exhibit distinct absorptions in the visible region, as shown in Fig. 4a. The absorption edges of pristine g-C₃N₄ and BiVO₄ nanosheet were located at around 460 and 530 nm, respectively. The blue-shifted light absorption of BiVO₄ compared with BiVO₄ in reference could be ascribed to the nanosheet structure of pristine BiVO₄ [27,39]. Tauc plots of BiVO₄ and g-C₃N₄ are shown in Fig. 4b. The band gap of g-C₃N₄ and BiVO₄ was calculated to be 2.7 eV and 2.34 eV, respectively, which is consistent with reported literature [40,41]. The absorption edge of the

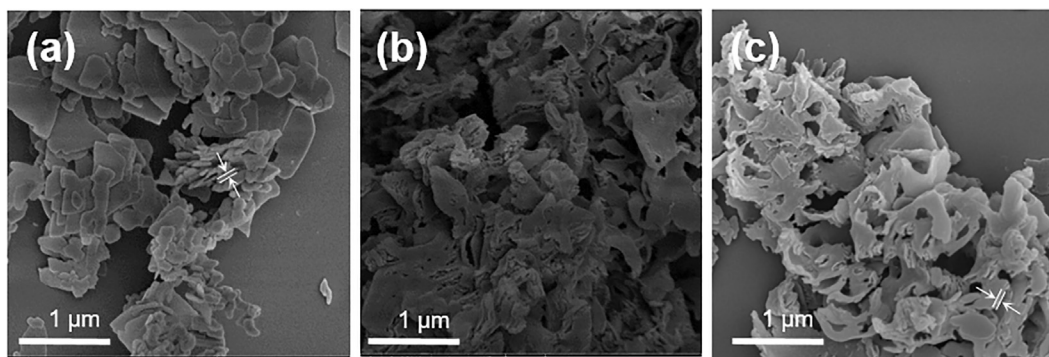


Fig. 2. SEM images of as-prepared BiVO₄ (a), g-C₃N₄(b), and BiVO₄/g-C₃N₄ (c).

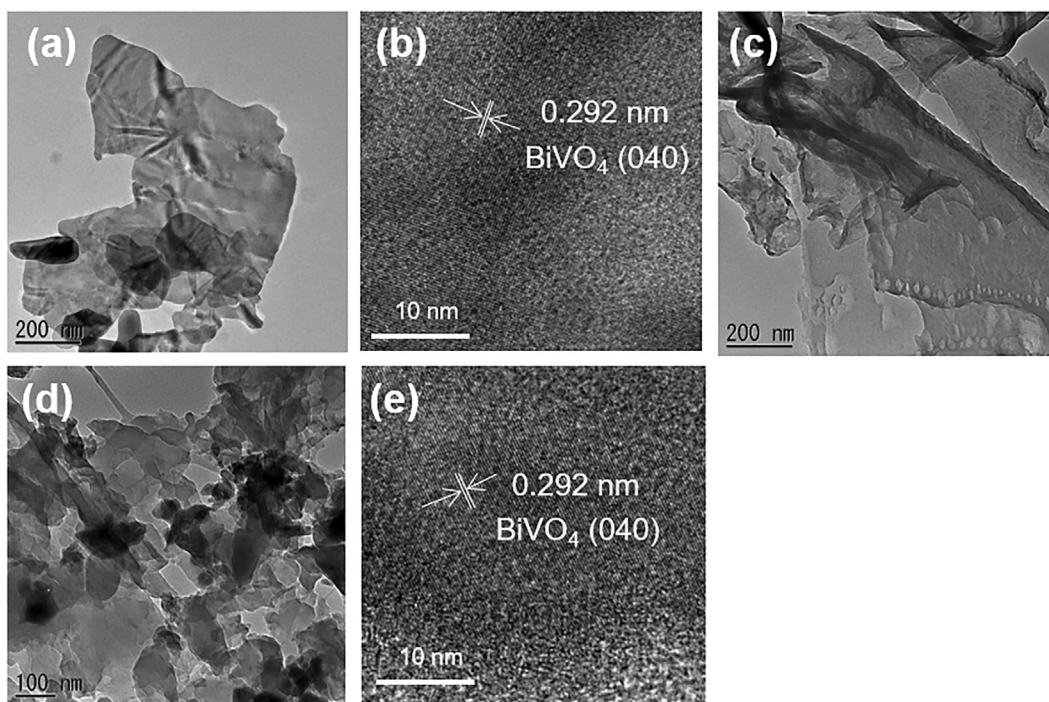


Fig. 3. TEM (a, c, and e) and HRTEM (b and d) images of as-prepared BiVO₄ (a and b), g-C₃N₄ (c), and BiVO₄/g-C₃N₄ (d and e).

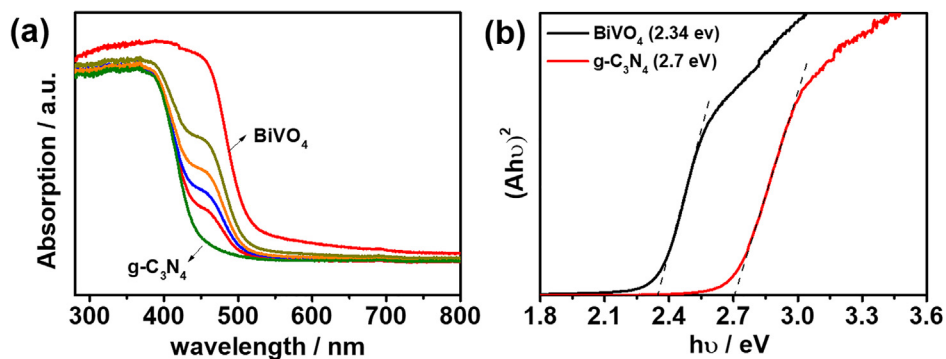


Fig. 4. UV-Vis DRS (a) and band gaps (b) of as-prepared BiVO₄, g-C₃N₄, and BiVO₄/g-C₃N₄.

fabricated sample with different compositions are distributed between those of pure BiVO₄ and g-C₃N₄ and increased from BiVO₄-5/g-C₃N₄ to BiVO₄-40/g-C₃N₄ in correlation to the increasing ratio of BiVO₄. The addition of BiVO₄ apparently expanded the

absorption edge of hybrid samples, due to that BiVO₄ could harvest more photon for its wider absorption edge.

The surface composition of BiVO₄ and g-C₃N₄ and strong interaction between the two materials was further verified by X-ray

photoelectron spectroscopy (XPS). Fig. 5(a) demonstrates that the peaks of C 1s centered at 285.9 and 289.0 eV were regarded as N=C=N [42] and C–O [43] functional groups, respectively. The two peaks located at the binding energies of 399.5 and 401.3 eV for the N 1s spectrum of g-C₃N₄ corresponded to the tertiary nitrogen N–(C)₃ groups and amino groups C–N–H [44,45] in the polymeric g-C₃N₄ structure (Fig. 5(b)), respectively. In the hybrid sample, by contrast, these bands of C and N spectra shift to a higher binding energy. Those shifts illustrate that g-C₃N₄ and BiVO₄ has a strong interaction during the catalytic that g-C₃N₄ and BiVO₄ has a strong interaction during the catalytic performance when hybridized with BiVO₄ nanosheets.

The XPS spectra of Bi species of the pristine BiVO₄ nanosheets, as shown in Fig. 5(c), display two main peaks (165.6 and 160.2 eV) with two shoulders peaks (161.9 and 167.2 eV), which suggests that the Bi exists in two different valence states i.e. Bi³⁺ and Bi²⁺ [46,47]. In Fig. 5(d), there are two fitted peaks at 517.7 and 519.5 eV in the V 2p core-level spectra, which could be attributed to the binding energy of V⁴⁺ and V⁵⁺ in terms of V2p_{3/2} orbital [48,49]. Thus, in contrast to the shift of C and N peak, the peaks of Bi and V in the nanosheets hybrid shifted to lower binding energy. These results suggest that the g-C₃N₄ of BiVO₄/g-C₃N₄ act as electron donors to achieve charge transfer and separation, resulting in an enhanced photocatalytic performance as compared to that of pure BiVO₄ and g-C₃N₄.

The photocatalytic RhB degradation was evaluated to measure the catalytic performance of as-prepared samples (Fig. 6a). Firstly, the dark adsorption equilibrium was established prior to the visible irradiation, and all of the solutions show nearly unchanged concentration after stirring for 30 min. The stability of RhB was also confirmed without any catalysts under the reaction condition. Pure BiVO₄ performed an inefficient degradation effect after photoreaction for 1 h, while g-C₃N₄ partially degraded RhB, and only 60% of RhB was removed after 1 h irradiation. The poor photocatalytic performance can be ascribed to the rapid recombination of photo-generated electron-hole pairs. All BiVO₄/g-C₃N₄ samples except BiVO₄-40/g-C₃N₄ showed improved photocatalytic activity.

Moreover, the BiVO₄-40/g-C₃N₄ exhibited an approximate level of degradation of g-C₃N₄, and an increased level of degradation of >80% was revealed of BiVO₄-5/g-C₃N₄ and BiVO₄-10/g-C₃N₄. Among them, BiVO₄-10/g-C₃N₄ performed the highest photocatalytic activity with a degradation rate of nearly 100% within 1 h. The performance of BiVO₄/g-C₃N₄ sample illustrated that there existed an optimum ratio between BiVO₄ and g-C₃N₄ for the best photocatalytic. This photocatalytic degradation of RhB suggests that the hybrid photocatalyst has remarkably increased the photocatalytic activity compared to those of both pristine BiVO₄ and g-C₃N₄. Thus, it is reasonable that the separation of the photo-induced electron-hole pairs through the formation of a composite with g-C₃N₄ nanosheet and BiVO₄ nanosheet leads to an enhanced photocatalytic performance.

The kinetics of RhB photocatalytic degradation using BiVO₄, g-C₃N₄, and BiVO₄/g-C₃N₄ samples were shown in Fig. 6b. The linear correlation between ln(C/C₀) and the reaction time (*t*) indicates that the degradation of RhB follows the apparent first-order kinetics [50,51]:

$$\ln(C_0/C) = kt$$

where C₀ is the initial concentration of the reactant (mg/L), C is the concentration of the reactant at time *t* (mg/L), *k* is the reaction rate constant (min⁻¹), *t* is reaction time (min). The corresponding degradation efficiency and *k* value were calculated in Table S1. When the BiVO₄ is employed as the photocatalyst, ca. 16.7% RhB molecules are decomposed after the visible-light irradiation proceeds for 60 min. The rate constant of the photocatalytic degradation in this case is estimated to be ca. 0.0026 min⁻¹. Meanwhile, when g-C₃N₄ is employed as the photocatalyst, ca. 45.7% RhB molecules are photodecomposed under the same experimental conditions, wherein the rate constant is estimated to be ca. 0.0096 min⁻¹. Among all of as-prepared samples, BiVO₄-10/g-C₃N₄ represented the highest performance with a degradation rate of ca. 91.5%, and the rate constant in this case is estimated to be ca. 0.0410 min⁻¹. This is ca. 15.8 and 4.3 times larger than that of pure BiVO₄ and g-C₃N₄, respectively, which shows that the appropriate proportion of BiVO₄/

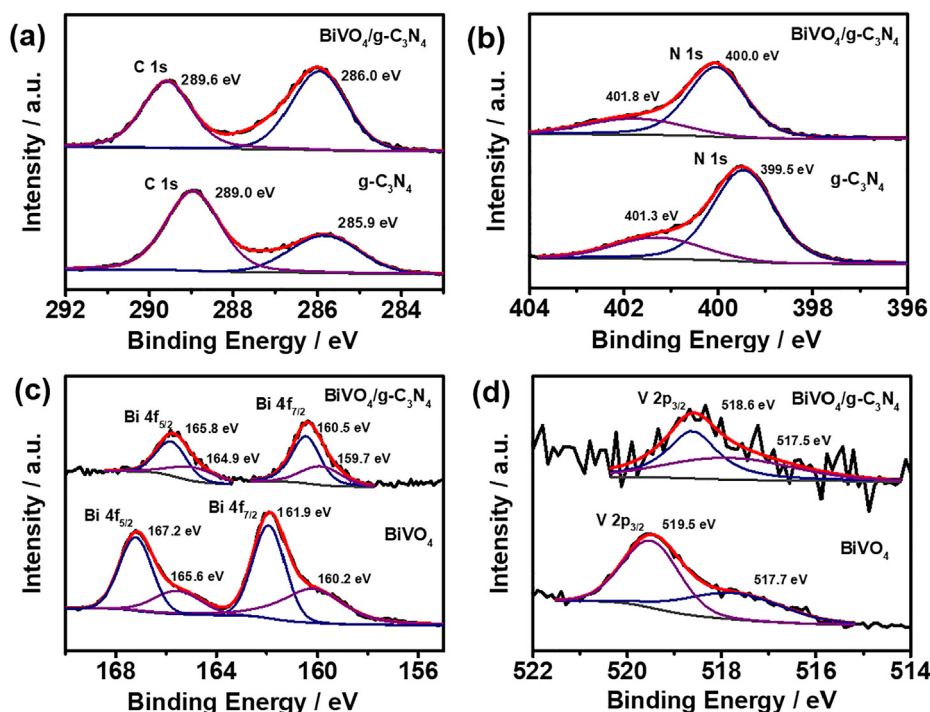


Fig. 5. High-resolution XPS spectra of C 1s (a) and N 1s (b) of as-prepared g-C₃N₄ and BiVO₄/g-C₃N₄; Bi 4f (c) and V 2p (d) of as-prepared BiVO₄ and BiVO₄/g-C₃N₄.

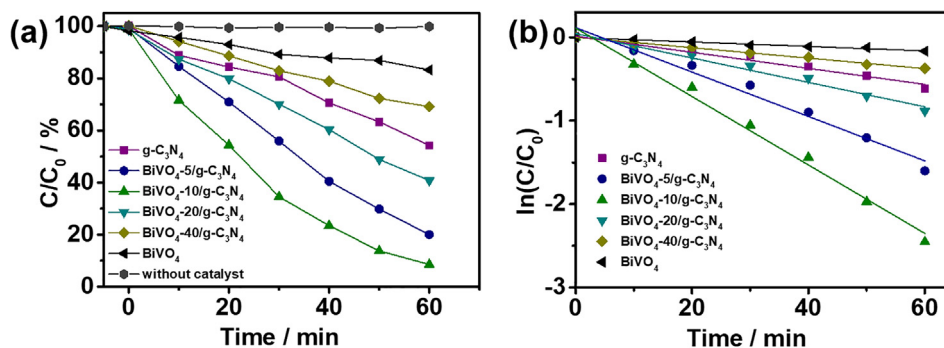


Fig. 6. (a) Photocatalytic activity of the as-prepared BiVO₄, g-C₃N₄, and BiVO₄/g-C₃N₄ photocatalysts for the photodegradation of RhB pollutant under visible light. (b) Kinetics of RhB degradation in solution by BiVO₄, g-C₃N₄, and BiVO₄/g-C₃N₄ samples based on the data in (a).

g-C₃N₄ composite with 2D/2D structure could enhanced the photocatalytic capability than that of pure BiVO₄ and g-C₃N₄.

The stability of the BiVO₄-10/g-C₃N₄ was also carried out by the cycling degradation of RhB to estimate the performance of a catalyst under visible light irradiation. As shown in Fig. S2, RhB was degraded close to zero within 60 min in each cycle and the activities were no obvious decrease within five cycles, suggesting that the hybrid sample acts as a stable photocatalyst for RhB degradation. Furthermore, it is generally accepted that 2D photocatalysts with high ratio of surface-to-volume can enhance the separation of photo-generated electron-hole pairs by charge transfer, and thus, the good stability of BiVO₄/g-C₃N₄ may due to the intimate face-to-face interface of 2D/2D structure and the reduction of charge recombination [8].

Photocatalytic oxygen production over the as-prepared BiVO₄/g-C₃N₄, g-C₃N₄, and BiVO₄ was performed under visible light (>420 nm) irradiation using 0.1 M AgNO₃ (4 mL) as electron acceptors to quench photo-induced electrons. The 5 wt% Co₃O₄ as a co-catalyst was used to reduce electron-hole recombination for oxygen generation. As shown in Fig. 7, the rate of O₂ generation on g-C₃N₄ and BiVO₄ was about 0.08 μmol h⁻¹ and 0.35 μmol h⁻¹, whereas, the rate of O₂ generation on BiVO₄/g-C₃N₄ is achieved to 0.97 μmol h⁻¹. The activity of BiVO₄/g-C₃N₄ in O₂ generation is increased by up to 12.1 and 2.8 times, comparing to that of pristine g-C₃N₄ and BiVO₄, respectively. There is no denying that 2D/2D structure can provide a large contact area, which serves as the interface for electron transfer between g-C₃N₄ and BiVO₄ [8]. Therefore, a suitable content of g-C₃N₄ with large contact interface is pivotal for enhancing the photocatalytic O₂ generation activity of BiVO₄/g-C₃N₄ composites.

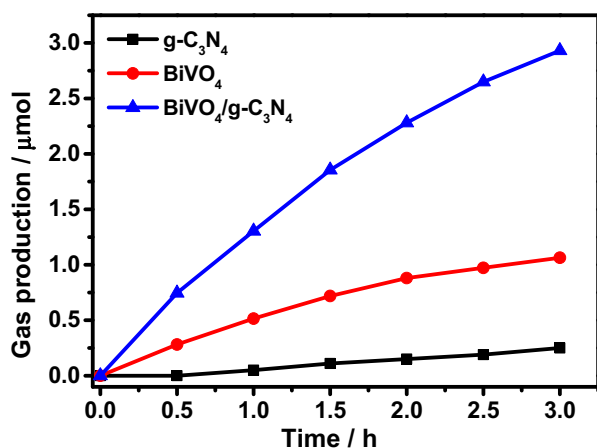


Fig. 7. Photocatalytic O₂ production from water with AgNO₃ as a sacrificial electron donor on as-prepared BiVO₄, g-C₃N₄, and BiVO₄/g-C₃N₄ catalysts under >420 nm light irradiation.

To illustrate this enhanced dyes degradation and O₂ generation performance, the photoelectrochemical properties of as-prepared samples are investigated. As shown in Fig. 8a, the photocurrents were measured at 0.6 V vs. Ag/AgCl under visible light irradiation for BiVO₄, g-C₃N₄, and BiVO₄/g-C₃N₄ nanosheets to investigate the electronic interaction between g-C₃N₄, and BiVO₄. It was clear that fast and obvious photocurrent responses were observed as soon as the light was turned on, while decayed to the baseline when the light was switched off [52,53]. The photo-responsive phenomenon was entirely reversible. Under visible light irradiation, BiVO₄ and g-C₃N₄ showed weak photocurrent response. On the contrary, BiVO₄/g-C₃N₄ photocatalyst showed a noticeable photocurrent under visible light irradiation (Fig. 8a). The photocurrent enhancement (5.6 and 2.8 times) of the BiVO₄/g-C₃N₄ nanosheets photocatalyst compared to pure BiVO₄ and g-C₃N₄, indicating an enhanced photo-induced electrons and holes separation, which could be attributed to the synergetic effect of 2D/2D materials between BiVO₄ and the g-C₃N₄.

EIS is also tested to explore the difference between BiVO₄, g-C₃N₄, and BiVO₄/g-C₃N₄ in the photo-generated electron transfer and the recombination of electrons and holes (Fig. 8b). It is generally assumed that a smaller semicircular arc in EIS represents the rapid interfacial charge transfer and efficient separation of the photo-generated electron-hole pairs [54]. The Nyquist plots of BiVO₄/g-C₃N₄ shows the smallest diameter, then following by g-C₃N₄ and BiVO₄ in sequence. The consequence further confirmed that the unique 2D/2D layered structure results in the lower charge transfer resistance occurred in the BiVO₄/g-C₃N₄ hybrid nanosheets due to the strong interaction between BiVO₄ and g-C₃N₄.

PL spectroscopy is also an efficient technique to characterize the charge separation, migration, and the extent of the recombination of photo-generated electron-hole pairs. It is reported that the rate of recombination is directly reflected in the PL emission intensity, and lower recombination rates result in lower emission intensities. As shown in Fig. S3, pure g-C₃N₄ shows the highest intensity of the PL spectra among all the samples, which confirms that there are some photo-generated electrons in g-C₃N₄ which prefer to recombine with holes rather than migrate onto the surface. However, the emission intensity is effectively curbed by compositing with BiVO₄, suggesting the low rate of recombination via electron transfer between BiVO₄ and g-C₃N₄. Consequently, the PL emission results are consistent with the photoelectrochemical data, which can be further correlated with electron transfer and the higher photocatalytic performance.

Based on the above analysis, the mechanism of the 2D/2D nanosheet composite with enhanced performance was explored (Scheme 1). The improved performance can be ascribed to matched conduction/valence band and suppress the electron-hole pair recombination between g-C₃N₄ and BiVO₄ [27]. Under the visible light irradiation, the electrons on the VB of both BiVO₄ and g-C₃N₄

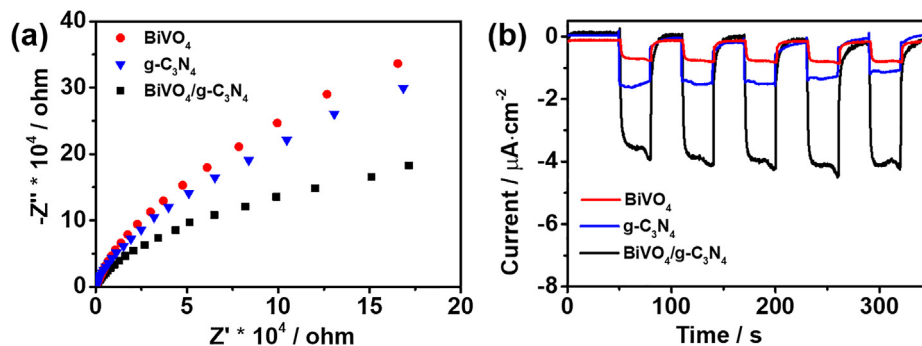
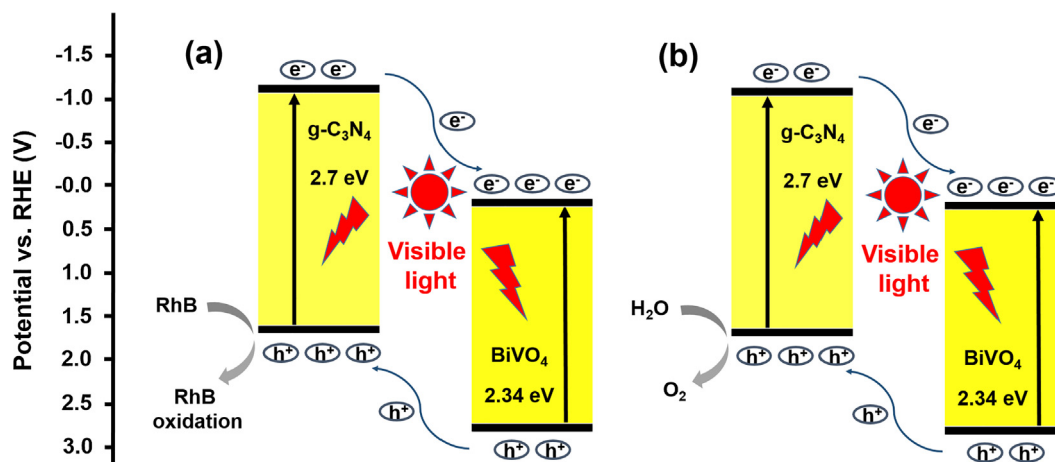


Fig. 8. (a) Transient photocurrent responses of as-prepared BiVO₄, g-C₃N₄, and BiVO₄/g-C₃N₄ in 0.5 M Na₂SO₄ aqueous solution electrolyte at 0.5 V vs Ag/AgCl under simulated solar light irradiation. (b) EIS Nyquist plots of as-prepared BiVO₄, g-C₃N₄, and BiVO₄/g-C₃N₄.



Scheme 1. Proposed Schematic of (a) Photodegradation of RhB, (b) Photocatalytic O₂-Production over the BiVO₄/g-C₃N₄ Nanosheet.

can be excited by the high energy photon. The photo-generated electrons from the CB of g-C₃N₄ could migrate to the surface of BiVO₄, in the meantime, the photo-induced holes from VB of BiVO₄ could transfer to the VB of g-C₃N₄. Therefore, the recombination processes between electron and hole was reduced, thus providing an enhanced photocatalytic performance [29,34]. The two-dimensional BiVO₄ and g-C₃N₄ nanosheet precursor could provide more contact area to promote synergetic effect, presented as a higher photocatalytic activity.

4. Conclusions

In conclusion, we have rationally developed a 2D multilayered nanostructure photocatalysts with various compositions of BiVO₄ and g-C₃N₄. The hybrid nanosheets exhibited excellent visible-light-driven photocatalytic performance as compared with pure g-C₃N₄ and BiVO₄, which derived from the fact that the two 2D nanostructure in the hybrid could easily contacting with each other to facilitate the electron-hole separation. After optimization the proportion of BiVO₄, BiVO₄-10/g-C₃N₄ exhibits an excellent RhB degradation and O₂ generation activity under visible light irradiation. This work may provide some inspiration for the fabrication of 2D/2D nanosheet heterostructures with efficient photocatalytic performance.

Acknowledgments

This work has been supported by Natural Science Foundation of China (21603024, 21577013, U1508205, and 21373037),

International S&T Cooperation Program of China (2016YFE010 9800), the Liaoning Province Doctor Startup Fund (201601038), and the Fundamental Research Funds for the Central Universities (DUT16ZD224).

Appendix A. Supplementary material

Supplementary data associated with this article can be found, in the online version, at <https://doi.org/10.1016/j.jcis.2018.08.071>.

References

- [1] H. Tong, S.X. Ouyang, Y.P. Bi, N. Umezawa, M. Oshikiri, J.H. Ye, *Adv. Mater.* 24 (2012) 229–251.
- [2] Y. Li, W.Q. Cui, L. Liu, R.L. Zong, W.Q. Yao, Y.H. Liang, Y.F. Zhu, *Appl. Catal. B: Environ.* 199 (2016) 412–423.
- [3] L. Liu, L. Ding, Y.G. Liu, W.J. An, S.L. Lin, Y.H. Liang, W.Q. Cui, *Appl. Catal. B: Environ.* 201 (2017) 92–104.
- [4] Y. Zhang, W.Q. Cui, W.J. An, L. Liu, Y.H. Liang, Y.F. Zhu, *Appl. Catal. B: Environ.* 221 (2018) 36–46.
- [5] F. Gauvin, V. Caprai, Q.L. Yu, H.J.H. Brouwers, *Appl. Catal. B: Environ.* 227 (2018) 123–131.
- [6] H.W. Huang, S.C. Tu, C. Zeng, T.R. Zhang, A.H. Reshak, Y.H. Zhang, *Angew. Chem., Int. Ed.* 56 (2017) 11860–11864.
- [7] A. Malathi, J. Madhavan, M. Ashokkumar, P. Arunachalam, *Appl. Catal. A* 555 (2018) 47–74.
- [8] W.J. Ong, *Front. Mater.* 4 (2017) 11.
- [9] Y.G. Li, X.L. Wei, X.Y. Yan, J.T. Cai, A.N. Zhou, M.R. Yang, K.Q. Liu, *Phys. Chem. Chem. Phys.* 18 (2016) 10255–10261.
- [10] J.Y. Hu, C.Y. Zhai, C.K. Yu, L.X. Zeng, Z.Q. Liu, M.S. Zhu, *J. Colloid Interface Sci.* 524 (2018) 195–203.
- [11] H. Wang, Y.H. Liang, L. Liu, J.S. Hu, P. Wu, W.Q. Cui, *Appl. Catal. B: Environ.* 208 (2018) 22–34.
- [12] J.Z. Liao, L.C. Chen, M.L. Sun, B. Lei, X.L. Zeng, Y.J. Sun, F. Dong, *Chin. J. Catal.* 39 (2018) 779–789.

- [13] J.Y. Hu, C.Y. Zhai, L.X. Zeng, Y.K. Du, M.S. Zhu, *Catal. Sci. Technol.* 8 (2018) 3562–3571.
- [14] F. Chen, Q. Yang, X.M. Li, G.M. Zeng, D.B. Wang, C.G. Niu, J.W. Zhao, H.X. An, T. Xie, Y.C. Deng, *Appl. Catal. B: Environ.* 200 (2017) 330–342.
- [15] J.Q. Wen, J. Xie, H.D. Zhang, A.P. Zhang, Y.J. Liu, X.B. Chen, X. Li, *ACS Appl. Mater. Inter.* 9 (2017) 14031–14042.
- [16] J.Q. Yan, H. Wu, H. Chen, L.Q. Pang, Y.X. Zhang, R.B. Jiang, L.D. Li, S.Z. Liu, *Appl. Catal. B: Environ.* 194 (2016) 74–83.
- [17] P. Niu, L.L. Zhang, G. Liu, H.M. Cheng, *Adv. Funct. Mater.* 22 (2012) 4763–4770.
- [18] X. Wang, Y.H. Liang, W.J. An, J.S. Hu, Y.F. Zhu, W.Q. Cui, *Appl. Catal. B: Environ.* 219 (2017) 53–62.
- [19] N. Tian, Y.H. Zhang, X.W. Li, K. Xiao, X. Du, F. Dong, G.I.N. Waterhouse, T.R. Zhang, H.W. Huang, *Nano Energy* 38 (2017) 72–81.
- [20] M.Q. Wen, T. Xiong, Z.G. Zang, W. Wei, X.T. Tang, F. Dong, *Opt. Exp.* 24 (2016) 10205–10212.
- [21] H.J. Kong, D.H. Won, J. Kim, S.I. Woo, *Chem. Mater.* 28 (2016) 1318–1324.
- [22] Y.H. Zheng, Y. Cheng, Y.S. Wang, F. Bao, L.H. Zhou, X.F. Wei, Y.Y. Zhang, Q. Zheng, *J. Phys. Chem. B* 110 (2006) 3093–3097.
- [23] Y. Zhao, R.G. Li, L.C. Mu, C. Li, *Cryst. Growth Des.* 17 (2017) 2923–2928.
- [24] X.D. Zhang, Y. Xie, *Chem. Soc. Rev.* 42 (2013) 8187–8199.
- [25] Y. Hou, J.Y. Li, Z.H. Wen, S.M. Cui, C. Yuan, J.H. Chen, *Nano Energy* 8 (2014) 157–164.
- [26] Q.G. Meng, H.Q. Lv, M.Z. Yuan, Z. Chen, Z.H. Chen, X. Wang, *ACS Omega* 2 (2017) 2728–2739.
- [27] Y.X. Ji, J.F. Cao, L.Q. Jiang, Y.H. Zhang, Z.G. Yi, *J. Alloys Compd.* 590 (2014) 9–14.
- [28] S. Samanta, S. Khilari, D. Pradhan, R. Srivastava, *ACS Sustain. Chem. Eng.* 5 (2017) 2562–2577.
- [29] F. Chen, Q. Yang, Y. Wang, J.W. Zhao, D.B. Wang, X.M. Li, Z. Guo, H. Wang, Y.C. Deng, C.G. Niu, G.M. Zeng, *Appl. Catal. B: Environ.* 205 (2017) 133–147.
- [30] R.Z. Sun, Q.M. Shi, M. Zhang, L.H. Xie, J.S. Chen, X.M. Yang, M.X. Chen, W.R. Zhao, *J. Alloys Compd.* 714 (2017) 619–626.
- [31] M. Ou, S.P. Wan, Q. Zhong, S.L. Zhang, Y. Song, L.N. Guo, W. Cai, Y.L. Xu, *Appl. Catal. B: Environ.* 221 (2018) 97–107.
- [32] X. Lin, D. Xu, Y. Xi, R. Zhao, L.N. Zhao, M.S. Song, H.J. Zhai, G.B. Che, L.M. Chang, *Colloids Surf. A* 513 (2017) 117–124.
- [33] Y. Wang, J.Y. Sun, J. Li, X. Zhao, *Langmuir* 33 (2017) 4694–4701.
- [34] J. Zhao, J.H. Yan, H.J. Jia, S.W. Zhong, X.Y. Zhang, L. Xu, *J. Mol. Catal. A* 424 (2016) 162–170.
- [35] W.Y. Wang, X.W. Wang, C.X. Zhou, B. Du, J.X. Cai, G. Feng, R.B. Zhang, *J. Phys. Chem. C* 121 (2017) 19104–19111.
- [36] L. Zhou, W.Z. Wang, S.W. Liu, L.S. Zhang, H.L. Xu, W. Zhu, *J. Mol. Catal. A* 252 (2006) 120–124.
- [37] J.S. Zhang, X.F. Chen, K. Takanabe, K. Maeda, K. Domen, J.D. Epping, X.Z. Fu, M. Antonietti, X.C. Wang, *Angew. Chem., Int. Ed.* 49 (2010) 441–444.
- [38] M. Seredych, T.J. Bandosz, *Carbon* 107 (2016) 895–906.
- [39] S. Obregon, A. Caballero, G. Colon, *Appl. Catal. B: Environ.* 117 (2012) 59–66.
- [40] G.G. Zhang, S.H. Zang, L.H. Lin, Z.A. Lan, G.S. Li, X.C. Wang, *ACS Appl. Mater. Interfaces* 8 (2016) 2287–2296.
- [41] Z. Zhou, Y.H. Li, K. Lv, X.F. Wu, Q. Li, J.M. Luo, *Mater. Sci. Semicond. Process.* 75 (2018) 334–341.
- [42] Y.F. Yang, J.J. Chen, Z.Y. Mao, N. An, D.J. Wang, B.D. Fahlman, *RSC Adv.* 7 (2017) 2333–2341.
- [43] C. Quiros, P. Prieto, A. Fernandez, E. Elizalde, C. Morant, R. Schlögl, O. Spillecke, J.M. Sanz, *J. Vac. Sci. Technol. A* 18 (2000) 515–523.
- [44] D.Q. Gao, Y.G. Liu, P.T. Liu, M.S. Si, D.S. Xue, *Sci. Rep.* 6 (2016) 35768.
- [45] K.L. He, J. Xie, Z.H. Yang, R.C. Shen, Y.P. Fang, S. Ma, X.B. Chen, X. Li, *Catal. Sci. Technol.* 7 (2017) 1193–1202.
- [46] C. Regmi, T.H. Kim, S.K. Ray, T. Yamaguchi, S.W. Lee, *Res. Chem. Intermed.* 43 (2017) 5203–5216.
- [47] J. Tian, Y.H. Sang, G.W. Yu, H.D. Jiang, X.N. Mu, H. Liu, *Adv. Mater.* 25 (2013) 5075–5080.
- [48] C. Regmi, Y.K. Kshetri, S.K. Ray, R.P. Pandey, S.W. Lee, *Appl. Surf. Sci.* 392 (2017) 61–70.
- [49] Z.X. Zhao, H.X. Dai, J.G. Deng, Y.X. Liu, C.T. Au, *Chin. J. Catal.* 34 (2013) 1617–1626.
- [50] M.N. Rashed, A.A. El-Amin, *Int. J. Phys. Sci.* 2 (2007) 73–81.
- [51] G.Z. Liao, S. Chen, X. Quan, H.T. Yu, H.M. Zhao, *J. Mater. Chem.* 22 (2012) 2721–2726.
- [52] M.S. Zhu, X.Y. Cai, M. Fujitsuka, J.Y. Zhang, T. Majima, *Angew. Chem., Int. Ed.* 56 (2017) 2064–2068.
- [53] N. Iqbal, I. Khan, Z.H. Yamani, A. Qurashi, *Sci. Rep.* 6 (2016) 32319.
- [54] C.Y. Zhai, M.S. Zhu, F.Z. Pang, D. Bin, C. Lu, M.C. Goh, P. Yang, Y.K. Du, *ACS Appl. Mater. Interfaces* 8 (2016) 5972–5980.